Neutron Radiography and Numerical Simulation of Mixing Behavior in a Reactor for Supercritical Hydrothermal Synthesis

Ken-ichi Sugioka, Kyohei Ozawa, and Takao Tsukada
Dept. of Chemical Engineering, Tohoku University, 6-6-07 Aramaki, Aoba-ku, Sendai 980-8579, Japan

Seiichi Takami
Institute of Multidisciplinary Research for Advanced Materials, Tohoku University, 2-1-1 Katahira, Aoba-ku, Sendai 980-8577, Japan

Tadafumi Adschiri
Institute of Multidisciplinary Research for Advanced Materials, Tohoku University, 2-1-1 Katahira, Aoba-ku, Sendai 980-8577, Japan

WPI Advanced Institute for Materials Research, Tohoku University, 2-1-1 Katahira, Aoba-ku, Sendai 980-8577, Japan

Katsumi Sugimoto and Nobuyuki Takenaka
Dept. of Mechanical Engineering, Kobe University, 1-1 Rokkodai, Nada, Kobe 657-8501, Japan

Yasushi Saito
Research Reactor Institute, Kyoto University, 2 Asashiro-Nishi, Kumatori-cho, Sennan-gun, Osaka 590-0494, Japan

DOI 10.1002/aic.14313
Published online December 29, 2013 in Wiley Online Library (wileyonlinelibrary.com)

We have visualized the distributions of temperature and water density in a tubular flow reactor for supercritical hydrothermal synthesis of nanoparticles by neutron radiography, and investigated the effect of reactor configuration on the mixing behavior in the reactor. Here, three types of reactors were used, and the mixing behaviors of supercritical water and room-temperature water at a T-junction in the reactors were observed. As a result, it was revealed that the distributions of temperature and water density in the tubular flow reactors strongly depend on their configurations by neutron radiography. In addition, numerical simulations have been carried out to investigate the flow patterns and temperature distributions in the reactor in detail using the commercial software FLUENT, and it was demonstrated that the numerical results can explain the experimental results obtained by neutron radiography well. © 2013 American Institute of Chemical Engineers *AIChE J*, 60: 1168–1175, 2014

Keywords: neutron radiography, numerical simulation, temperature distributions, tubular flow reactor, supercritical hydrothermal synthesis

Introduction

Hydrothermal synthesis under supercritical conditions, namely, supercritical hydrothermal synthesis, is a useful method of producing metal oxide nanoparticles from metal salt aqueous solutions.[1,2] The high reaction temperature and the properties of supercritical water as a reaction medium make the reaction rate quite high and the solubility of dehydrated products extremely low. Consequently, a rapid increase in the degree of supersaturation, very high nucleation rates, and the mass production of nanoparticles can be achieved. In such a supercritical hydrothermal synthesis process, continuous flow reactors, in which two streams of metal salt aqueous solution and heated water are mixed under supercritical conditions, are commonly used.[1,3] Rapid and uniform mixing of the streams is indispensable to produce metal oxide nanoparticles, and the size and distributions of these nanoparticles are strongly affected by how the reactants and supercritical water streams are mixed in the reactor.[4–6] Therefore, various experimental and computational studies have been performed to visualize and understand the mixing of streams in the reactor under supercritical conditions. In experimental studies, model fluids for mimicking the properties of water under supercritical conditions[7,8] or transparent sapphire cells that allow optical observation under high-temperature and high-pressure conditions[9] have been used to understand the mixing behavior in a reactor for supercritical hydrothermal synthesis. Recently, tomographic x-ray methods have been applied to image the formation of CeO_2 nanoparticles in the interior of a hydrothermal synthesis reactor.[10] Numerical simulations have also been carried out to study the flow dynamics of supercritical water in flow

Correspondence concerning this article should be addressed to T. Tsukada at tsukada@pcel.che.tohoku.ac.jp.

reactors, and the relationship between the mixing behavior determined from numerical simulations and the size and shape of the nanoparticles determined from experiments was investigated under various conditions including reactor configuration.[11–22] Although such previous experimental and numerical works provided various types of valuable information, there remain several problems, including difficulties in experimentally reproducing the real reactor configuration used for the actual production of nanoparticles and in verifying the numerical results of the complicated flow behavior near the critical point of water.

The scattering of neutrons has been utilized in various fields to visualize the internal structures of objects.[23,24] Although x-rays have higher permeability toward lighter elements, neutrons can penetrate materials with heavier elements and are mostly scattered by hydrogen atoms. Therefore, neutron radiography, that is, the imaging of the internal structure of an object by measuring the intensity of scattered neutrons, is suitable for visualizing the density of water inside a tubular flow reactor used for supercritical hydrothermal synthesis and made of stainless steel. Using neutron radiography, Peterson et al.[25–27] have studied salt precipitation in supercritical water and the flow pattern in a reverse-flow vessel for salt precipitation, whereas Balaskó et al.[28] have revealed the behavior of supercritical water in a container. However, no study entailing the *in situ* observation of the mixing behavior in a tubular flow reactor for the supercritical hydrothermal synthesis of nanoparticles has yet been carried out. Recently, for the first time, we have performed neutron radiography on a tubular flow reactor of 1/4-in. diameter for supercritical hydrothermal synthesis, and visualized the mixing behavior of supercritical water and room-temperature water at a T-junction.[29] The results showed that the difference in density between supercritical water and room-temperature water, as well as how the density changed during mixing, was clearly visualized by neutron radiography. The density-stratified flow in the side tube feeding room-temperature water was also visualized.

In this work, we performed both neutron radiography experiments and numerical simulations on the mixing behavior in a 1/8-in. diameter flow reactor. In our experiments, the effects of reactor configuration and the flow rates of room-temperature water and supercritical water on the mixing behavior were discussed. The measurement of the neutron mass attenuation coefficient in water at various temperatures enabled quantitative evaluation of the temperature distributions in the reactor. In the numerical simulations, we observed the flow patterns and temperature distributions in the reactor in detail using the commercial software FLUENT and compared the numerical results with the experimental results obtained by neutron radiography.

Experimental

Supercritical hydrothermal reactor

For the *in situ* observation of the mixing behavior in supercritical hydrothermal synthesis, a tubular flow reactor with a T-junction was used to mix a stream of heated water with another stream of room-temperature water. Figure 1a shows a schematic diagram of the experimental apparatus, where the two streams in the T-junction were set to the three directions shown in Figure 1b. The T-junction was comprised of a Swagelok union tee and SUS316 tubes whose outer diameter and

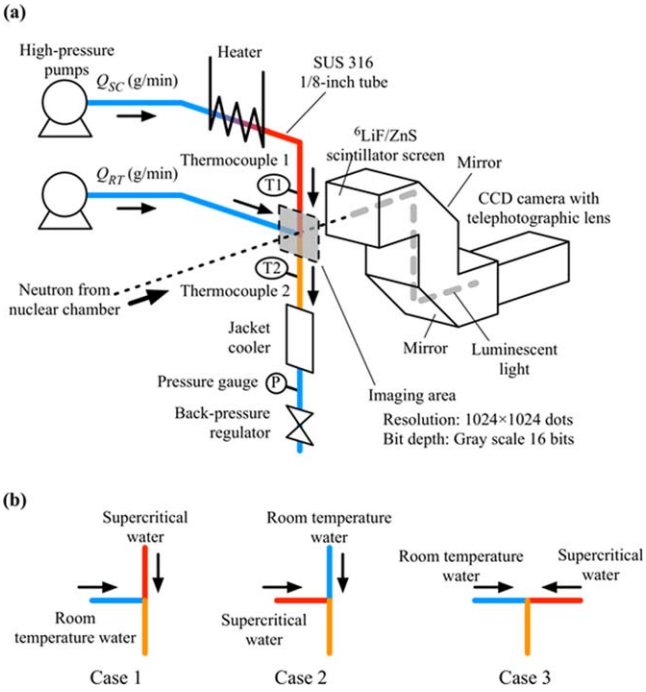

Figure 1. (a) Schematic diagram of experimental apparatus and (b) reactor configurations used in this study.

[Color figure can be viewed in the online issue, which is available at wileyonlinelibrary.com.]

wall thickness were 1/8 in. and 0.71 mm, respectively, and covered by a thermal insulator. The inner diameter of the union tee piece was 2.3 mm. The reactor configuration in Case 1 is the same as that in our previous work[29] except for the size of the tubular reactor, that is, 1/4-in. diameter in our previous work. A high-pressure pump (Nihon Seimitsu Kagaku, NP-KX-540) supplied deionized water at rates Q_{SC} of 8.0 and 12.0 g/min; this water was then heated using a furnace up to approximately 390°C just before mixing. The other pump supplied deionized water at room temperature at rates Q_{RT} of 1.0–6.0 g/min. As, in this work, room-temperature water without metal ion precursors was used, hydrothermal reactions did not occur. The two streams were mixed at the T-junction, after which the mixed stream was quenched using a jacket cooler and released from a back-pressure regulator (TESCOM, 26-1700 Series) that maintained the pressure at approximately 25 MPa. The above setup was almost identical to those we used to synthesize metal oxide nanoparticles, except for the supplied fluid, that is, water instead of metal ion solutions. The Reynolds numbers of the streams before and after mixing are summarized in Table 1.

Neutron radiography

Neutron radiography is an imaging technique in which a neutron beam is used to visualize the internal structure of objects. In this work, we used a thermal neutron beam emitted from the B4 port of the Kyoto University Reactor (KUR) at the Research Reactor Institute, Kyoto University. KUR was operated at either 1 or 5 MW with a neutron flux of about 1 or 5×10^7 n/cm^2 s, respectively, at the beam exit of the B4 neutron guide tube. Hydrogen has high mass attenuation coefficients, and thus is opaque against neutrons. In contrast, heavier elements including iron, nickel, and chromium are more transparent. Therefore, we can visualize the density

Table 1. Reynolds Numbers of the Streams Before and After Mixing

	Q_{SC} (g/min)	Q_{RT} (g/min)	Re (SCW)	Re (RTW)	Re (mixed)
Case 1	8.0	1.0	2.4×10^3	12	1.6×10^3
	8.0	2.0	2.4×10^3	25	1.3×10^3
	8.0	4.0	2.6×10^3	49	1.9×10^3
	12.0	1.5	4.8×10^3	19	2.8×10^3
	12.0	3.0	4.8×10^3	37	3.2×10^3
	12.0	6.0	4.8×10^3	74	3.2×10^3
Case 2	8.0	2.0	2.8×10^3	25	1.6×10^3
	8.0	4.0	2.8×10^3	49	1.6×10^3
	12.0	3.0	4.2×10^3	29	2.5×10^3
Case 3	8.0	2.0	2.8×10^3	25	1.7×10^3
	8.0	4.0	2.8×10^3	49	1.7×10^3

of water inside the stainless-steel container using a neutron beam. The neutron beam passing through the mixing part was converted by a ^{6}LiF/ZnS scintillator screen (Fuji Electric Co.) into luminescent light, which in turn was monitored by a charge-coupled device (CCD) camera (PIXIS-1024B, Princeton Instruments Co.) equipped with a telephotographic lens that was deliberately located off the neutron beam axis to avoid direct exposure to neutron irradiation, as shown in Figure 1. A square area of 3.3×3.3 cm^2 around the mixing part was monitored by the CCD camera and converted into a 16-bit gray-scale image with a resolution of 1024×1024 pixels. The typical periods used to obtain a single image were 30 s at 1 MW and 6 s at 5 MW. The obtained image was processed as described below.

Data analysis

We obtained six images, that is, I_i (j, k): $1 \le i \le 6$, $1 \le j, k \le 1024$, by neutron radiography under each set of experimental conditions, where j and k indicate the location of a pixel in the horizontal and vertical directions, respectively, in the ith image. Because the attenuation length of neutrons possibly changes with temperature, we applied the following analysis method for images that was different from that used in the previous work.[29]

1. The bright spots that randomly appear as noise in the images were removed as follows. Here, an image (I'_i) was produced by selecting the smaller value from the ith (I_i) and $(i+1)$th (I_{i+1}) images, that is

$$I'_i(j,k) = \min\{I_i(j,k), I_{i+1}(j,k)\} \text{ for } 1 \le j,k \le 1024 \quad (1)$$

and then a single image, I (j, k), without the bright spots was obtained by summing the five images produced.

2. Using both a dark current image (I_b) without irradiating the neutron beam taken to remove background noise and an image without the objective of visualization (I_0) to identify the original intensity distribution of the neutron beam on the imaging area, the Beer–Lambert law gives the following equation for the total absorbance of the neutron beam, A_{total}

$$A_{total}\,(=\mu_m \rho t + A) = -\ln \frac{I - I_b}{I_0 - I_b} \quad (2)$$

Here, μ_m, ρ, t, and A, respectively, represent the mass attenuation coefficient of water (cm^2/g), the density of water (g/cm^3), the thickness of the water layer along the direction of the neutron beam (cm), and the absorbance by the reactor, that is, the solid section of the objective.

3. As the absorbance by the reactor, A, in Eq. 2 is obtained from a neutron radiographic image of the reactor filled with air, $I_{reactor}$, as

$$A = -\ln \frac{I_{reactor} - I_b}{I_0 - I_b} \quad (3)$$

the distribution of $\mu_m \rho t$ (j, k) in the image is given as

$$\mu_m \rho t = -\ln \frac{I - I_b}{I_0 - I_b} + \ln \frac{I_{reactor} - I_b}{I_0 - I_b} \quad (4)$$

Because of the thermal expansion of the reactor, the position might change depending on temperature. In such a case, the image of the empty reactor, $I_{reactor}$, shrank, rotated, and moved to fit with the image of the reactor under experimental conditions.

4. Using a neutron radiographic image of the reactor filled with water at room temperature, I_{RT}, a similar equation for water density at room temperature ρ_{RT} is obtained

$$\mu_{m,RT}\,\rho_{RT}\,t = -\ln \frac{I_{RT} - I_b}{I_0 - I_b} + \ln \frac{I_{reactor} - I_b}{I_0 - I_b} \quad (5)$$

Here, $\mu_{m,RT}$ represents the mass attenuation coefficient of water at room temperature.

5. As the ratio of Eq. 4–5 gives the distributions of $\left(\mu_m \rho / \mu_{m,RT}\,\rho_{RT}\right)$ in the reactor, the temperature distributions of water in the reactor can be obtained using the relationship between T and $\mu_m \rho$ described below. If the distribution of water density is necessary, the relationship between T and ρ[30] should be used.

Calibration curve of temperature-attenuation coefficient

To obtain the relationship between T and the ratio of attenuation coefficient $\left(\mu_m \rho / \mu_{m,RT}\,\rho_{RT}\right)$ described in the previous section, the apparatus, which consists of a thermally insulated SUS304 tube with a 1/4-in. diameter and a 10-cm height and two thermocouples inserted from the inlet and outlet of the tube, was replaced with a tubular flow reactor with a T-junction in Figure 1. Then, neutron radiographic images of water flowing inside the tube were taken while varying the temperature of water from 25 to 420°C at 25 MPa and analyzed by the same procedure as that described in the previous section. T is the average temperature of the two thermocouples facing each other set at a distance of 40 mm inside the tube. Figure 2 shows the measured relationship between T and $\mu_m \rho$, where the error bars represent the uncertainty of attenuation coefficient measurement, that is, the standard deviation of attenuation coefficient measured. In this work, the uncertainty was large because of small neutron flux, and consequently, the temperatures determined from Figure 2 were dispersed as the isotherms in the following figures (Figures 4–8) show.

Numerical simulations

Numerical simulations of the three-dimensional (3-D) unsteady flow and temperature fields in a tubular flow reactor shown in Figure 1 were carried out using the commercial software FLUENT 12.1. Figure 3 shows the physical model of the tubular flow reactor. Here, the room-temperature water meets the supercritical water at the T-junction, and then the resulting fluid mixture is cooled down to approximately room temperature using a heat exchanger.

The temperature and pressure dependences of the thermophysical properties of water, that is, density, viscosity,

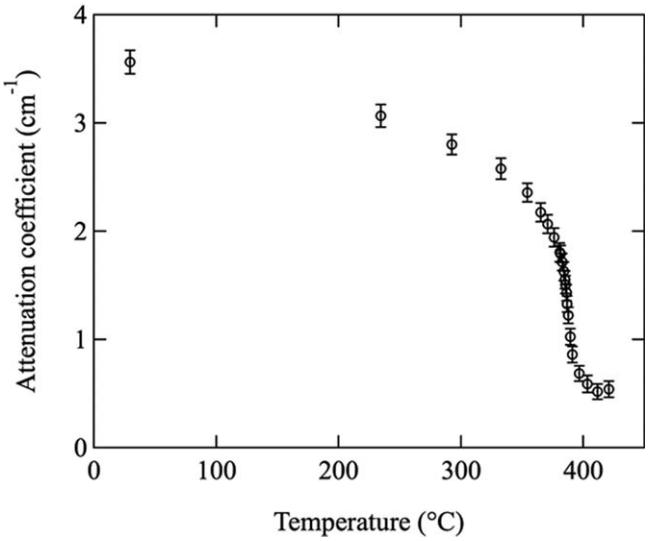

Figure 2. Attenuation coefficient $\mu_m\rho$ of water at 25 MPa as a function of temperature.

thermal conductivity, and specific heat, were obtained from the National Institute of Standards and Technology (NIST) database,[30] and the properties were introduced into FLUENT as a piecewise-polynomial function of temperature.

The boundary conditions for the velocity field are given as follows: fully developed parabolic velocity profiles were given at two inlets for the supercritical water and room-temperature water, a nonslip boundary condition was set at the solid wall, and a traction-free boundary condition was set at the outlet.

In addition, the following boundary conditions were given for a temperature field. The temperatures at the two inlets were fixed, a zero normal gradient condition was applied at the outlet, and an adiabatic condition was given at the solid wall except for the heat exchanger wall where the heat-transfer coefficient and ambient fluid temperature were considered to be 400 W/m^2 K and 280 K, respectively.

The tetrahedral meshes, whose total numbers were 2,102,246, were used. The time increment was 10^{-5} s.

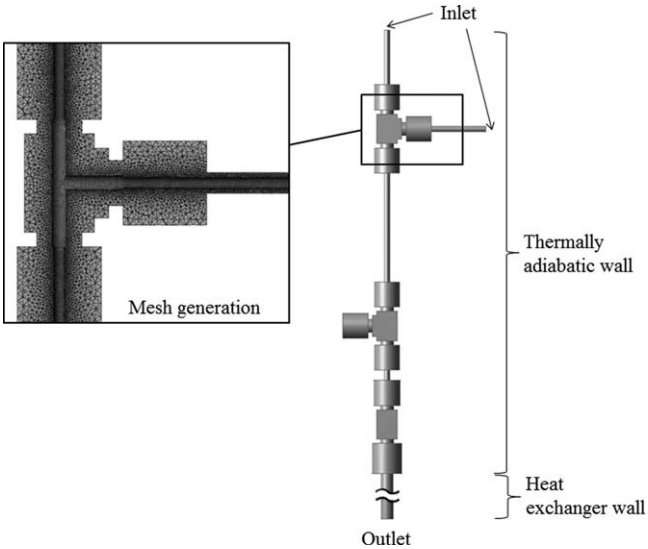

Figure 3. Flow reactor and meshes adopted in numerical simulation.

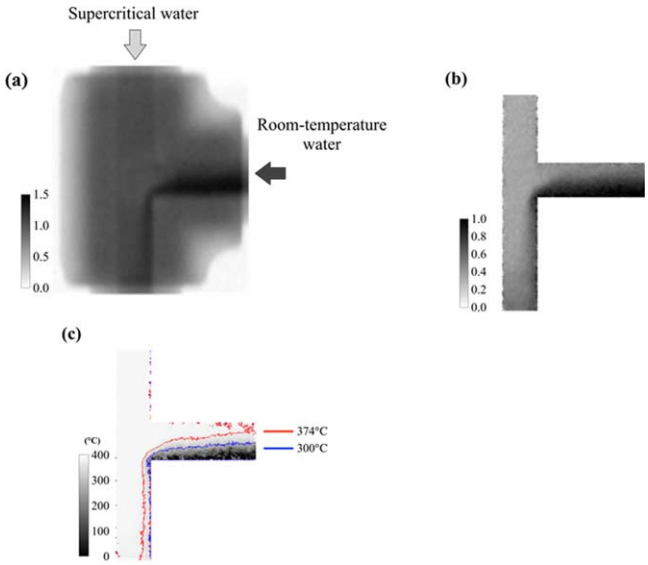

Figure 4. Distributions of (a) total absorbance of neutron beam, (b) attenuation coefficient ratio, and (c) temperature around T-junction.

[Color figure can be viewed in the online issue, which is available at wileyonlinelibrary.com.]

Results and Discussion

Experimental results

Figure 4a shows an image of the total absorbance of the neutron beam, A_{total}, around the T-junction in the tubular reactor (Case 1 in Figure 1), when the flow rates of supercritical water and room-temperature water, Q_{SC} and Q_{RT}, were 8.0 and 2.0 g/min, respectively, and the temperature of supercritical water at Thermocouple 1 in Figure 1 was 385°C. In this image, the darker area indicates the greater scattering of neutrons, that is, the region where high-density, low-temperature water was flowing. Figures 4b, c show the distributions of the attenuation coefficient ratio $\left(\mu_m\rho/\mu_{m,RT}\,\rho_{RT}\right)$ and the temperature T obtained from the image analysis described in the previous section, respectively.

Figure 5 shows the effect of the flow rate of room-temperature water, Q_{RT}, on the distributions of (a) temperature and (b) water density around the T-junction in the reactor whose configuration corresponds to Case 1 in Figure 1, when the flow rate of supercritical water, Q_{SC}, was 8.0 g/min. Here, the distributions of water density were evaluated using the relationship between temperature and water density in the NIST database.[30] The figures reveal that low-temperature, high-density water is flowing from right to left in the horizontal tube and then downward near the wall of the vertical tube. The supercritical water with a lower density flows from the top toward the bottom of the vertical tube, coming into contact with the lower-temperature water at the T-junction. In addition, it is confirmed that a density-stratified layer was generated by the inflow of supercritical water into the top of the side tube owing to buoyancy. Comparing the results for three different flow rates, Q_{RT}, the layer thickness of low-temperature water flowing along the wall of the vertical tube increases, and thus the average temperature in the downstream region decreases as Q_{RT} increases. The degree of density stratification in the horizontal tube also becomes weaker with Q_{RT}.

Similarly to that shown in Figure 5, the effect of Q_{RT} on the distributions of temperature and water density in the tubular

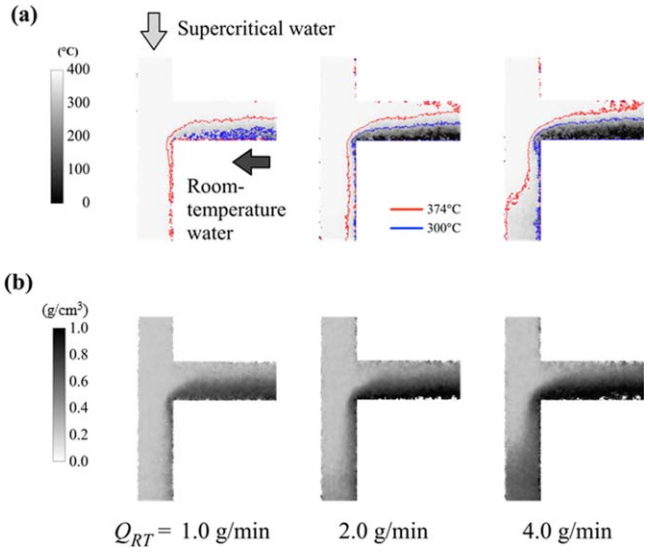

Figure 5. (a) Temperature and (b) water density profiles around the T-junction in Case 1 when $Q_{SC} = 8$ g/min.

[Color figure can be viewed in the online issue, which is available at wileyonlinelibrary.com.]

reactor in Case 1 is shown in Figure 6, where the flow rate of supercritical water, Q_{SC}, was 12.0 g/min, but the ratios of Q_{RT} to Q_{SC} were the same as those in Figure 5. The temperature of the supercritical water was 393°C, which is higher than 385°C in Figure 5. According to the NIST database,[30] the densities of water at 385 and 393°C are 313 and 194 kg/m^3 at 25 MPa, respectively. By comparing the results in Figures 5 and 6 for the same flow rate ratio, the degree of density stratification in the horizontal tube in Figure 6 is lower than that in Figure 5, in spite of the higher temperature and lower density of supercritical water in Figure 6. This is due to a larger amount of room-temperature water flowing through the horizontal tube. In particular, the whole region inside the horizontal tube for $Q_{RT} = 6$ g/min is occupied by subcritical water.

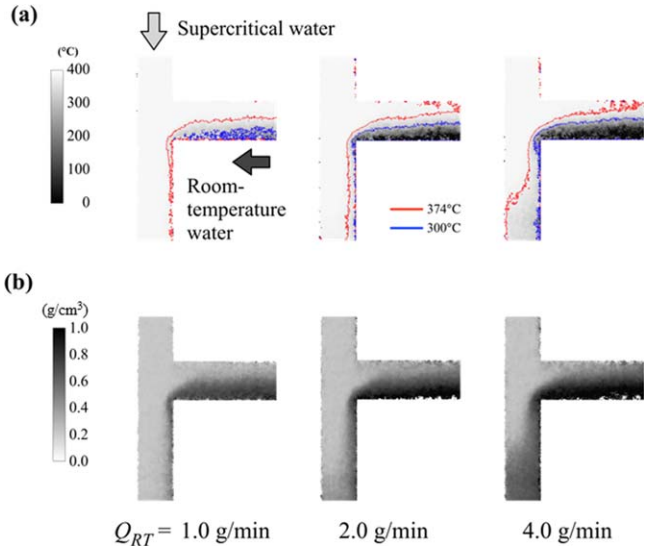

Figure 6. (a) Temperature and (b) water density profiles around the T-junction in Case 1 when $Q_{SC} = 12$ g/min.

[Color figure can be viewed in the online issue, which is available at wileyonlinelibrary.com.]

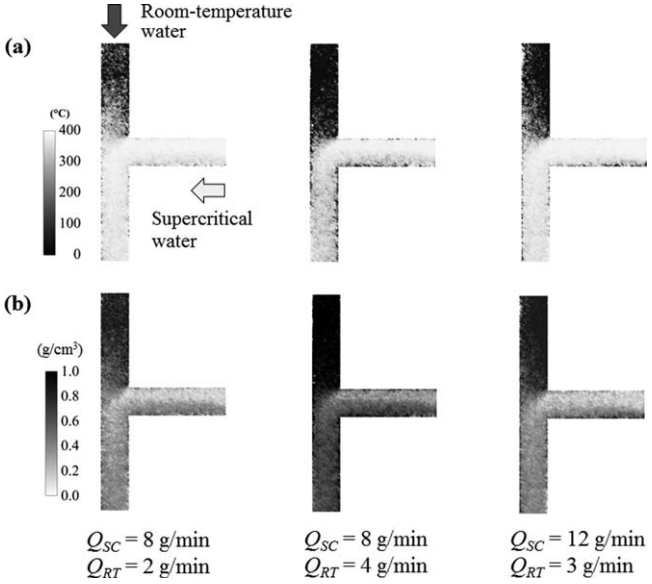

Figure 7. (a) Temperature and (b) water density profiles around the T-junction in Case 2 when $Q_{SC} = 8$ g/min.

Figure 7 shows the effect of the flow rate of room-temperature water Q_{RT} on the distributions of (a) temperature and (b) water density around the T-junction in the reactor in Case 2 shown in Figure 1. Here, the room-temperature water flows downward at $Q_{RT} = 2$ and 4 g/min, and the supercritical water whose temperature is 386–387°C is injected into the T-junction from the side of the tube at $Q_{SC} = 8$ g/min. The directions of these streams are opposite to those in Figures 5 or 6. From Figure 7a, it can be seen that the temperature in the region above the T-junction at $Q_{RT} = 2$ g/min is higher than that at $Q_{RT} = 4$ g/min throughout the cross-sectional area of the tube; consequently, the water density in the tube at $Q_{RT} = 2$ g/min is lower than that at $Q_{RT} = 4$ g/min, as shown in Figure 7b. Also, the temperature in the downstream region for $Q_{RT} = 4$ g/min becomes lower. In the case where the room-temperature water flows downward at a lower rate and the supercritical water flows into the T-junction from the side at a higher rate, it can be inferred that the buoyancy convection can be easily generated at the T-junction owing to the density difference between the two fluid streams. Such convective mixing of room-temperature water and supercritical water might make the temperature above the T-junction higher and uniform throughout the cross-sectional area of the tube. This will be demonstrated numerically in the next section. Moreover, from Figure 7b, it is found that a density-stratified layer is generated in the horizontal tube, although the degree of stratification is lower than that in Figure 5. In Figure 7, the distributions of temperature and water density at $Q_{RT} = 3$ g/min and $Q_{SC} = 12$ g/min, respectively, are also shown. Although the ratios of Q_{RT} to Q_{SC} are the same, the mixing effect due to the buoyancy convection above the T-junction for $Q_{SC} = 12$ g/min becomes weaker because of the increase in the flow rate of the room-temperature water compared with the results for $Q_{SC} = 8$ g/min.

Figure 8 shows the distributions of (a) temperature and (b) water density in the reactor in Case 3 shown in Figure 1, where the room-temperature water and supercritical water are fed horizontally from the left and right sides to the T-junction, and then the resulting fluid mixture flows downward

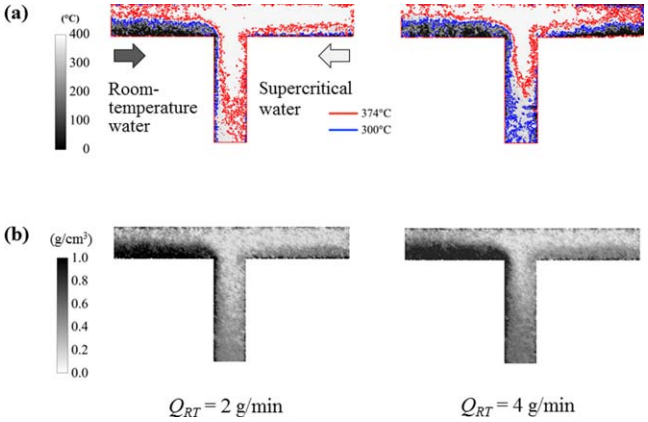

Figure 8. (a) Temperature and (b) water density profiles around the T-junction in Case 3 when Q_{SC} = 8 g/min.

[Color figure can be viewed in the online issue, which is available at wileyonlinelibrary.com.]

in the vertical tube. The flow rates of the room-temperature water, Q_{RT}, are 2 and 4 g/min, respectively, and that of the supercritical water, Q_{SC}, whose temperature is 387–388°C is 8 g/min. From the figures, the supercritical water with a lower density intrudes above the room-temperature water in the left horizontal tube, and then a density-stratified layer is generated in the tube. The degree of stratification becomes higher as the flow rate of the room-temperature water decreases. Moreover, in the right horizontal tube, the density-stratified layer is generated, although the degree of stratification is much weaker than that on the left side.

Blood et al.[7] have carried out flow visualization with model fluids in tubular flow reactors whose configurations were the same as those in this work, that is, Cases 1–3 in Figure 1, where methanol and 40% w/w aqueous sucrose solution were used as pseudosupercritical water and pseudo-metal salt solution, respectively, at room temperature. The present results obtained by neutron radiography for all three reactor configurations shown in Figures 5–8 qualitatively coincide with the visualization images by Blood et al.[7]

Numerical results

In the previous section, it was demonstrated that we can visualize the mixing behavior of room-temperature water and supercritical water, as well as the distributions of temperature and water density in a tubular flow reactor used for the supercritical hydrothermal synthesis of nanoparticles by using neutron radiography. However, it is not easy to understand the details of flow patterns and temperature distributions in the reactor by this method. Therefore, 3-D numerical simulations of flow and thermal fields in the reactor have been carried out using the commercial software FLUENT in this work.

Figure 9 shows the numerical results of the (a) temperature distributions and (b) stream lines in the tubular reactor for two different flow rates of the room-temperature water, that is, Q_{RT} = 2 and 4 g/min, when Q_{SC} = 8 g/min and the inlet temperature of the supercritical water T_{SC} = 387°C. These conditions are the same as those used to obtain the experimental results shown in Figure 5. The numerical results for both Q_{RT} are in the steady state. Although the calculated temperature distributions in Figure 9a are those in the cross section including the central axes of both the vertical and horizontal tubes, the measured distributions in Figure 5 are the average temperatures in the thickness direction of the water layer along the neutron beam because the temperatures were obtained from the relationship between temperature and the attenuation coefficient of neutrons passing through the water inside the tube, as mentioned in the previous section. Although the comparison between Figures 5 and 9a might not be strict, it is found that the numerical results at both Q_{RT} values can explain the temperature distributions in the experiments well. It can also be recognized that a density-stratified layer is generated in the horizontal tube from the numerical results of the temperature distributions in the radial direction of the horizontal tube. From Figure 9b, the supercritical water with a higher temperature and a lower density, which flows downward through the vertical tube, intrudes above the room-temperature water in the horizontal tube and returns to the T-junction owing to the flow of the room-temperature water. Such a vortex flow at the upper position of the horizontal tube might cause the formation of a density-stratified layer. In addition, the downward stream lines below the T-junction gently drift to the side of the wall to which the horizontal tube is connected, and a stagnation region of the flow exists on the opposite side of the wall where a vertical temperature gradient is generated, as shown in Figure 9a.

Figure 10a shows the numerical results of the temperature distributions in the tubular reactor for Q_{RT} = 2 g/min, Q_{SC} = 8 g/min, and T_{SC} = 387°C, where the room-temperature water flows downward in the vertical tube, while the supercritical water is injected into the T-junction through the horizontal tube similarly to that shown in Figure 7. The thermal field in the reactor, particularly just above the

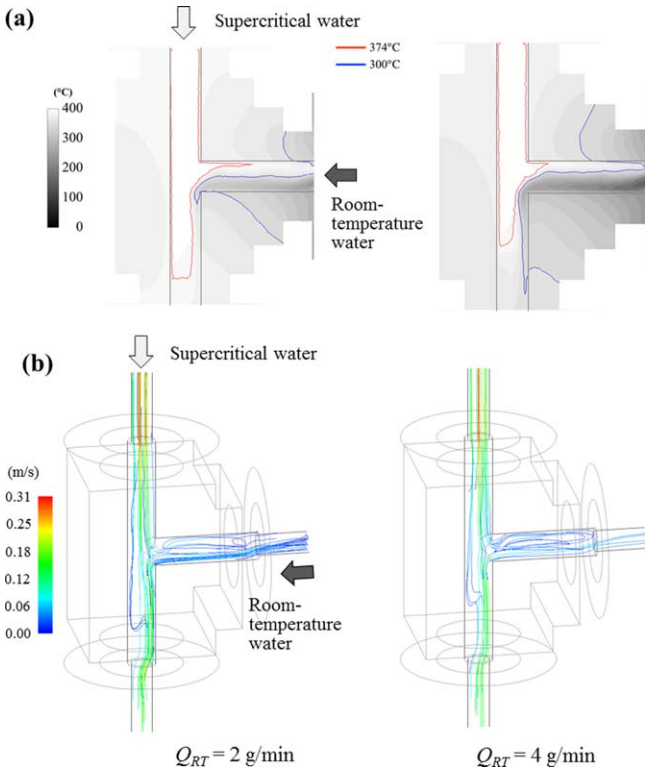

Figure 9. (a) Calculated temperature profiles and (b) stream lines around the T-junction in Case 1, when Q_{SC} = 8 g/min.

[Color figure can be viewed in the online issue, which is available at wileyonlinelibrary.com.]

T-junction, is time-dependent, as the four snapshots after the reference time t_0 represent. The lower-temperature water meanders downward through the vertical tube above the T-junction, and simultaneously, the higher-temperature water ascends and descends, that is, the vortex flow appears along the downward stream, as shown in Figure 10b. This is an unsteady-state flow caused by the coexistence of forced convection and buoyancy convection due to the density difference between the room-temperature water and the supercritical water. Also, it is found from Figure 10b that the stagnation region of the flow exists along the side of the wall as well as at the lower part of the horizontal tube where a density-stratified layer is generated as the experimental results in Figure 7b show. In addition, comparing the numerical distributions of average temperatures for 60 s in Figure 10c with Figure 7a, it can be seen that the thermal field above the T-junction in Figure 7a, that is, the higher temperature and its uniform distributions throughout the cross-sectional area of the tube, is caused by buoyancy convection as shown in Figure 10b.

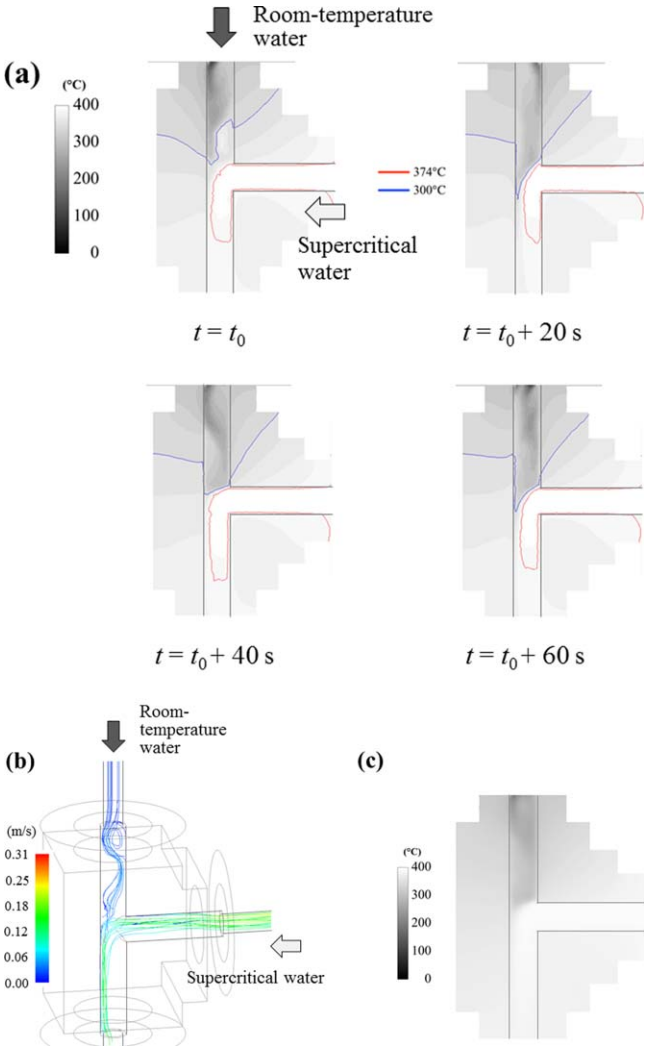

Figure 10. (a) Calculated time variations of temperature profiles, (b) stream lines, and (c) average temperature for 60 s around the T-junction in Case 2, when $Q_{RT} = 2$ g/min and $Q_{SC} = 8$ g/min.

[Color figure can be viewed in the online issue, which is available at wileyonlinelibrary.com.]

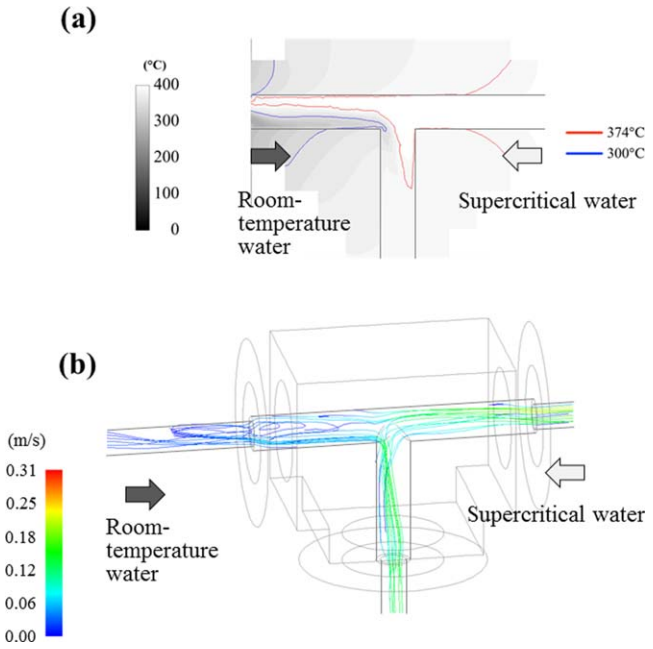

Figure 11. (a) Calculated temperature profiles and (b) stream lines around the T-junction in Case 3, when $Q_{RT} = 2$ g/min and $Q_{SC} = 8$ g/min.

[Color figure can be viewed in the online issue, which is available at wileyonlinelibrary.com.]

Figure 11 shows the numerical results of the (a) temperature distributions and (b) stream lines in the tubular reactor in Case 3, where the room-temperature water and supercritical water are fed horizontally from the left and right sides to the T-junction. The numerical results here are in a steady state. The flow rate of the room-temperature water, Q_{RT}, is 2 g/min, the rate of the supercritical water, Q_{SC}, is 8 g/min, and the inlet temperature of the supercritical water, T_{SC}, is 387°C. The high-temperature supercritical water intrudes above the room-temperature water in the left horizontal tube as shown in Figure 11b, and then a density-stratified layer is generated in the tube. By comparing the two isotherms in Figure 11a with those in Figure 8a, it is found that the numerical results can explain the temperature field in the tubular reactor well.

Conclusions

In this work, we have visualized the distributions of temperature and water density in a tubular flow reactor with a T-junction of 1/8-in. outer diameter used for supercritical hydrothermal synthesis by neutron radiography, and investigated the effect of the reactor configuration on the mixing behavior in the reactor. The configurations investigated here are as follows: in Case 1, the higher-temperature supercritical water flows from the top toward the bottom of the vertical tube, coming in contact with the lower-temperature water injected through the horizontal tube at the T-junction. In Case 2, the directions of the two fluid streams are opposite to those in Case 1. In Case 3, both streams are fed through the horizontal tubes to the T-junction. From the visualization using neutron radiography, it is found that density-stratified layers are generated in the horizontal tubes around the T-junction in Cases 1 and 3 in the flow rate ranges of the supercritical water and room-temperature water in this work. In contrast, buoyancy convection due to the density

difference between the two fluid streams is generated at the T-junction in Case 2; consequently, the convective mixing of the supercritical water and room-temperature water makes the temperature above the T-junction higher and uniform throughout the cross-sectional area of the tube. In addition, numerical simulations have been carried out to investigate the flow patterns and temperature distributions in the reactor in detail using the commercial software FLUENT, and it was demonstrated that the numerical results can explain the experimental results obtained by neutron radiography well. However, the quality of data obtained in this work was not sufficient to suggest the design strategies of the mixing piece. We believe that combining the results of neutron radiography, numerical simulation, and experimental studies where metal oxide nanoparticles were synthesized at the same conditions as those in neutron radiography, we can discuss how the mixing affects the produced nanoparticles and the design rule of mixing piece.

Acknowledgments

This research was supported in part by JPSP KAKENHI Grant Number 24656461 and by Nippon Sheet Glass Foundation for Materials Science and Engineering. This work has been carried out in part under the Visiting Researchers Program of Kyoto University Research Reactor Institute. The authors thank Hisashi Komeda of Kobe University for his helping in *in situ* observation experiment by neutron radiography.

Literature Cited

1. Byrappa K, Adschiri T. Hydrothermal technology for nanotechnology. *Prog Cryst Growth Charact Mater*. 2007;53:117–166.
2. Adschiri T, Lee Y-W, Goto M, Takami S. Green materials synthesis with supercritical water. *Green Chem*. 2011;13:1380–1390.
3. Hakuta Y, Hayashi H, Arai K. Fine particle formation using supercritical fluids. *Curr Opin Solid State Mater Sci*. 2003;7:341–008.
4. Adschiri T, Takami S, Umetsu M, Ohara S, Tsukada T. Hydrothermal synthesis of functional nanoparticles: process and properties. *Powder Sci Eng*. 2004;36:59–69 (in Japanese).
5. Byrappa K, Ohara S, Adschiri T. Nanoparticles synthesis using supercritical fluid technology—towards biomedical applications. *Adv Drug Deliv Rev*. 2008;60:299–327.
6. Toft LL, Aarup DF, Bremholm M, Hald P, Iversen BB. Comparison of T-piece and concentric mixing systems for continuous flow synthesis of anatase nanoparticles in supercritical isopropanol/water. *J Solid-State Chem*. 2009;182:491–495.
7. Blood P, Denyer J, Azzopardi B, Poliakoff M, Lester E. A versatile flow visualisation technique for quantifying mixing in a binary system: application to continuous supercritical water hydrothermal synthesis (SWHS). *Chem Eng Sci*. 2004;59:2853–2861.
8. Lester E, Blood P, Denyer J, Giddings D, Azzopardi B, Poliakoff M. Reaction engineering: the supercritical water hydrothermal synthesis of nano-particles. *J Supercrit Fluids*. 2006;37:209–214.
9. Aizawa T, Masuda Y, Minami K, Kanakubo M, Nanjo H, Smith RL. Direct observation of channel-tee mixing of high-temperature and high-pressure water. *J Supercrit Fluids*. 2007;43:222–227.
10. Middelkoop V, Boldrin P, Peel M, Buslaps T, Barnes P, Darr JA, Jacques SDM. Imaging the inside of a continuous nanoceramic synthesizer under supercritical water conditions using high-energy synchrotron X-radiation. *Chem Mater*. 2009;21:2430–2435.
11. Aimable A, Muhr H, Gentric C, Bernard F, Le Cras F, Aymes D. Continuous hydrothermal synthesis of inorganic nanopowders in supercritical water: towards a better control of the process. *Powder Technol*. 2009;190:99–106.
12. Demoissona F, Arianea M, Leybrosa A, Muhrb H, Bernard F. Design of a reactor operating in supercritical water conditions using CFD simulations. Examples of synthesized nanomaterials. *J Supercrit Fluids*. 2011;58:371–377.
13. Khokhar ZHI, Al-Harthi MA. Numerical and experimental studies of mixing of high temperature critical water. *Int J Eng Technol*. 2009; 9:119–123.
14. Masuda Y, Aizawa T, Suzuki A. Flow visualization and numerical simulation of T-junction mixing of high-temperature high-pressure water. *J Chem Eng Jpn*. 2009;42:64–70.
15. Wakashima Y, Suzuki A, Kawasaki S, Matsui K, Hakuta Y. Development of a new swirling micro mixer for continuous hydrothermal synthesis of nano-size particles. *J Chem Eng Jpn*. 2007;40:622–629.
16. Sierra-Pallares J, Alonso E, Montequi I, Cocero MJ. Particle diameter prediction in supercritical nanoparticle synthesis using three-dimensional CFD simulations. Validation for anatase titanium dioxide production. *Chem Eng Sci*. 2009;64:3051–3059.
17. Kawasaki S, Sue K, Ookawara R, Wakashima Y, Suzuki A. Development of novel micro swirl mixer for producing fine metal oxide nanoparticles by continuous supercritical hydrothermal method. *J Oleo Sci*. 2010;59:557–562.
18. Kawasaki S, Sue K, Ookawara R, Wakashima Y, Suzuki A, Hakuta Y, Arai K. Engineering study of continuous supercritical hydrothermal method using a T-shaped mixer: experimental synthesis of NiO nanoparticles and CFD simulation. *J Supercrit Fluids*. 2010;54:96–102.
19. Sue K, Sato T, Kawasaki S, Takebayashi Y, Yoda S, Hiaki T. Continuous hydrothermal synthesis of Fe2O3 nanoparticles using a central collision-type micromixer for rapid and homogeneous nucleation at 673 K and 30 MPa. *Ind Eng Chem Res*. 2010;49:8841–8846.
20. Sue K, Kawasaki S, Suzuki M, Hakuta Y, Hayashi H, Arai K, Takebayashi Y, Yoda S, Furuya T. Continuous hydrothermal synthesis of Fe2O3, NiO, and CuO nanoparticles by superrapid heating using a T-type micro mixer at 673 K and 30 MPa. *Chem Eng J*. 2011;166:947–953.
21. Sokmen CN. Effect of property variations on the mixing of laminar supercritical water streams in a T-junction. *Int Commun Heat Mass Transfer*. 2011;38:85–92.
22. Sierra-Pallares J, Marchisio DL, Alonso E, Parra-Santos MT, Castro F, Cocero MJ. Quantification of mixing efficiency in turbulent supercritical water hydrothermal reactors. *Chem Eng Sci*. 2011;66: 1576–1589.
23. Spowart AS. Neutron radiography. *J Phys E: Sci Instrum*. 1972;5: 497–510.
24. Strobl M, Manke I, Kardjilov N, Hilger A, Dawson M, Banhart J. Advances in neutron radiography and tomography. *J Phys D: Appl Phys*. 2009;42:243001-1–243001-21.
25. Peterson AA, Vontobel P, Vogel F, Tester JW. In situ visualization of the performance of a supercritical-water salt separator using neutron radiography. *J Supercrit Fluids*. 2008;43:490–499.
26. Peterson AA, Vontobel P, Vogel F, Tester JW. Normal-phase dynamic imaging of supercritical-water salt precipitation using neutron radiography. *J Supercrit Fluids*. 2009;49:71–78.
27. Peterson AA, Tester JW, Vogel F. Water-in-water tracer of supercritical-water reversing jets using neutron radiography. *J Supercrit Fluids*. 2010;43:250–257.
28. Balaskó M, Horváth L, Horváth A, Tóth P. Study of the behavior of supercritical water by dynamic neutron radiography. *Nucl Instrum Methods Phys Res A*. 2009;605:138–141.
29. Takami S, Sugioka K, Tsukada T, Adschiri T, Sugimoto K, Takenaka N, Saito Y. Neutron radiography on tubular flow reactor for hydrothermal synthesis: In situ monitoring of mixing behavior of supercritical water and room-temperature water. *J Supercrit Fluids*. 2012;63:46–51.
30. NIST database, Available at http://webbook.nist.gov/chemistry/fluid/. Accessed Dec. 21, 2013.

Manuscript received July 23, 2013, and revision received Oct. 9, 2013.